



Article

A Tool for Evaluating the Performance of SiC-Based Bidirectional Battery Chargers for Automotive Applications

Giuseppe Aiello ¹, Mario Cacciato ², Francesco Gennaro ¹, Santi Agatino Rizzo ^{2,*},
Giuseppe Scarcella ² and Giacomo Scelba ²

¹ STMicroelectronics, 95129 Catania, Italy; giuseppe.aiello01@st.com (G.A.); francesco.gennaro@st.com (F.G.)

² Department of Electrical, Electronics and Computer Engineering, University of Catania, 95129 Catania, Italy; mario.cacciato@unict.it (M.C.); giuseppe.scarcella@unict.it (G.S.); giacomo.scelba@unict.it (G.S.)

* Correspondence: santi.rizzo@unict.it

Received: 5 November 2020; Accepted: 14 December 2020; Published: 20 December 2020



Abstract: In this paper, a procedure to simulate an electronic power converter for control design and optimization purposes is proposed. For the addressed application, the converter uses SiC-MOSFET technology in bidirectional battery chargers composed of two power stages. The first stage consists of a single-phase AC/DC power factor correction synchronous rectifier. The following stage is a DC/DC dual active bridge. The converter has been modulated using a phase-shift technique which is able to manage bidirectional power flows. The development of a model-based simulation approach is essential to simplify the different design phases. Moreover, it is also important for the final validation of the control algorithm. A suitable tool consisting of a system-level simulation environment has been adopted. The tool is based on a block diagram design method accomplished using the Simulink toolbox in MATLABTM.

Keywords: automotive; battery charger; circuit modelling; power electronics; SiC MOSFET

1. Introduction

Powertrain electrification of electric vehicles (EVs) and plug-in hybrid vehicles (PHVs) has gained the attention of governments, media and the public as a possible alternative mode of supplying power to transport vehicles due to its inherent efficiency advantages, e.g., less CO₂ emissions, in comparison with internal combustion engine vehicles [1,2]. EVs are key elements for the worldwide upgrade to sustainable energy systems. On the one hand, they directly affect the transition to environmentally friendly transportation. On the other, they are useful for compensating for the effects of dispersed generation based on renewable energy resources [3]. In more detail, when the power available from these generators surpasses the local load, it may be necessary to cut the exceeding power to avoid misoperation conditions, or worse yet, service continuity reductions. This limitation in green energy utilization can be overcome with EVs, since they involve an increment in the local load. Moreover, they can be used as energy storage systems which are able to mitigate fluctuations in primary energy resources and, more generally, are useful when coping with optimal power flow [4].

As a consequence of the diffusion of EVs and PHVs, an increasing number of connections to the public electrical grid of smart on- and off-board battery chargers has occurred [5]. These components are of fundamental importance for managing the energy flows between vehicles and the AC grid. Recently, a new EV operating mode, called Vehicle to Grid (V2G), was proposed [6]. V2G enables the use of the EVs as distributed large energy storage systems connected to the grid when parked [7]. The reward for providing ancillary services makes V2G economically convenient which, in turn,

enables a wider diffusion of EVs, leading to environmental benefits [8]. On the other hand, the control strategy must take battery degradation into account [9].

Several bidirectional battery chargers (BBCs) for V2G have been already treated in the literature to investigate viable methods to achieve a compact, efficient and inexpensive solution. In [10,11], two designs of single-phase on-board BBCs were proposed, aiming to show the feasibility of reactive power support to the utility grid. In particular, [11] deals with the advantage of using wide band-gap semiconductor devices at high frequencies to reduce the current ripple by implementing both hardware and control solutions, similar to those adopted in converters for fuel cell power units [12]. In [13], a simple and functional BBC topology for stationary application was introduced. This topology was specifically designed to enhance the capabilities of a joint operation with an energy management system exploiting a storage stage in a residential environment. A literature analysis highlighted the fact that a key issue is to design and test a suitable control strategy. More specifically, the evaluation of the modulation, as well as of some features (e.g., current ripple and load step response), requires proper testing of the control strategy in dynamic conditions on small-time scales. On the other hand, appropriate long-timescale tests to evaluate the energy management capabilities of BBCs must be also performed. In some works [10–14], the development of a feasible converter model was needed to fulfil the specifications through a proper system design, optimizing the structure of the control strategy as well as the correct setting of the parameters for the controllers.

As in many physical system designs, the use of advanced computer-aided design (CAD) systems is important at different project stages [15]. At the beginning, they enable component sizing verification; subsequently, they are useful for offline control validation with uP-based simulators [16], where they are very helpful when applying a user-friendly GUI based simulation interface [17]. Other solutions which are increasingly being adopted in the industry are powerful real-time emulation systems based on FPGA, that are widely used both in power converters [18] and electrical drives applications [19,20], and are particularly useful for the study and testing of dangerous situations, such as systems faults [21].

In this framework, a proper design using an advanced simulator model is proposed in this paper. It enables the evaluation of the feasibility and the performance of the converter using CAD. This approach makes it possible to validate the operation of the BBC in both V2G and Grid to Vehicle (G2V) operating modes. The main contribution of this paper is to propose a tool with which to optimize the BBC design before constructing the converter prototype. Additionally, the model of SiC MOSFET power devices was integrated to exploit their advantages in BBCs. Indeed, such an approach can be useful for the optimal design of other converters in automotive applications. Finally, a mock-up was realized and tested, obtaining valuable results. In detail, the converter investigated was a 5-kW, single-phase BBC with two conversion stages: an active front end (AFE) PWM rectifier and a cascade-connected dual active bridge (DAB) with high-frequency isolation. Such an architecture was adopted for its bidirectional power flow, galvanic isolation, high efficiency in a wide operating range and reduced size and weight. The last features are due to the high switching frequency reached thanks to the use of SiC MOSFET power devices [22]. Every apparatus connected to the grid has to meet the power quality standards; therefore, the converter first stage also included power factor correction (PFC) capability. Figure 1 shows a flowchart of the overall tool.

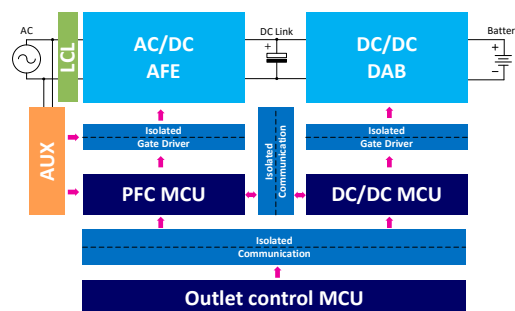


Figure 1. Overall picture of the evaluation tool.

2. Modelling the Bidirectional Battery Charger

For the application of a single-phase BBC, the proposed converter consists of two stages exploiting three H-bridges with modularity in the power board arrangement. Power devices with the same voltage breakdown should be used since the input and output voltage levels are similar. In this case, the three H-bridges can be identical, thus simplifying the converter design for the proposed converter that exploits identical SiC devices. As shown in Figure 2, the first stage is an AFE connected to the grid through an LCL filter which is useful to ensure both the power quality and the control of the power exchanged with the grid, while the second stage consists of a DAB converter.

The control strategy of the AC/DC converter is composed of a hierarchic control. On the one hand, it regulates the bidirectional power exchange with the grid. On the other, it shapes the current in a sinusoidal waveform. Hence, it consists of an inner loop current control in continuous conduction mode (CCM). The control is implemented on the dq rotating reference frame and is synchronous with the grid voltage. There is an outer loop to maintain constant the DC voltage, V_{DC} , using linear regulators, i.e., standard industrial proportional-integral (PI) control. As usual, the DAB is modulated in phase-shift. In this way, the control algorithm sets a suitable phase-shift for application between the switching signals of the two active bridges while maintaining the duty cycle of every switching pattern at 50%. Such a strategy makes it possible to achieve zero voltage switching (ZVS) upon turning on all of the DAB power switches, thereby increasing the converter efficiency. The phase-shift value sets the energy flow: in G2V mode, the energy flows towards the battery, while in V2G mode, the energy flow is directed from the battery to the AC grid.

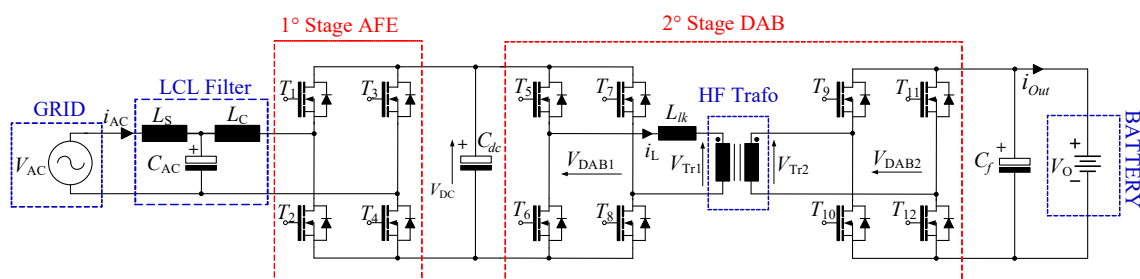


Figure 2. Converter topology. The first stage is the Active Front-End Rectifier; the second stage is the Dual Active Bridge.

2.1. Active Front-End Rectifier

The AFE, or synchronous rectifier, is connected via a filter to the utility grid where it performs AC/DC conversion and PFC [23,24]. Figure 3 shows the circuit test-bench emulator implementation using the Simulink Simscape Electrical Toolbox, a typical AFE control strategy based on the voltage oriented control algorithm. Park transformation is considered to obtain the best performance, e.g., zero error in steady-state and high control dynamics [25].

Park transformation is used to convert the two-phase stationary frame (α - β^*) (1) into the two-phase rotating frame (d-q) which is synchronous with the grid voltage phase θ (2). The two-phase voltages in reference to the dq reference frame are converted in stationary quantities α - β using the inverse matrix of the reference frame transformation [26]:

$$\begin{cases} L \frac{di_\alpha}{dt} + Ri_\alpha = V_{t\alpha} - V_{s\alpha} \\ L \frac{di_\beta}{dt} + Ri_\beta = V_{t\beta} - V_{s\beta} \end{cases} \quad (1)$$

$$\begin{cases} L \frac{di_d}{dt} + Ri_d - \omega(t)Li_q = V_{td} - V_{sd} \\ L \frac{di_q}{dt} + Ri_q + \omega(t)Li_d = V_{tq} - V_{sq} \\ \frac{d\theta}{dt} = \omega(t) \end{cases} \quad (2)$$

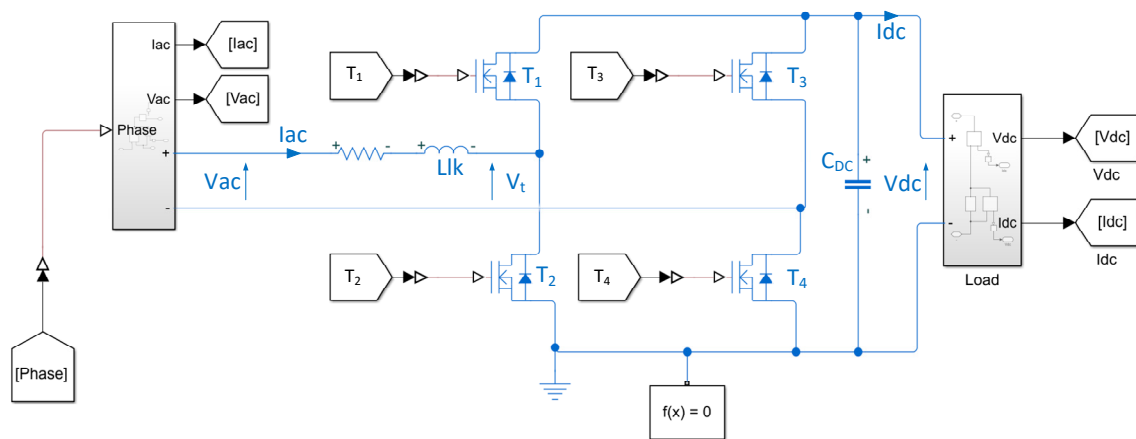


Figure 3. AC Stage—Implementation of the Active Rectifier in Simscape electrical Simulink.

The terms i_d, i_q and ρ are state variables, while V_{td}, V_{tq} and $\omega(t)$ are control variables. In particular, ω represents the control variable referring to the synchronous reference frame.

This model shows the nonlinearities related with the terms $\omega(t)Li_d$ and the sinusoidal components of the AC system: $V_{sd} = \hat{V}_S \cos(\omega_0 t + \theta_0 - \rho)$, $V_{sq} = \hat{V}_S \sin(\omega_0 t + \theta_0 - \rho)$.

Using this modelling approach, the purpose of the control is the cancellation of the sinusoidal terms; a phase locked loop “PLL” algorithm is used for this purpose. Applying the AC voltage as the input, the PLL output is $\rho(t) = \omega_0 t + \theta_0$, and Equation (2) turns to Equation (3), which contains only DC quantities in steady-state.

$$\begin{cases} L \frac{di_d}{dt} = \omega_0 Li_q - Ri_d + V_{td} - \hat{V}_S \\ L \frac{di_q}{dt} = -\omega_0 Li_d - Ri_q + V_{tq} \end{cases} \quad (3)$$

$$\begin{aligned} P_S(t) &= \frac{3}{2} [V_{sd}(t)i_d(t) + V_{sq}(t)i_q(t)] \\ Q_S(t) &= \frac{3}{2} [-V_{sd}(t)i_q(t) + V_{sq}(t)i_d(t)] \end{aligned} \quad (4)$$

$$\begin{aligned} P_S(t) &= \frac{3}{2} [V_{sd}(t)i_d(t)] \\ Q_S(t) &= -\frac{3}{2} [V_{sd}(t)i_q(t)] \end{aligned} \quad (5)$$

In V2G applications, the goal is to suitably manage the flow of active and reactive powers, according to Equation (4). By estimating the phase angle of the AC system through the PLL and imposing $V_{sq} = 0$, it follows that it is possible to rewrite the power relationships given in Equation (4) according to Equation (5), where the coupling terms have been cancelled.

Since in dq-axis, the component V_{sd} is constant, from Equation (5), it is evident that it is possible to obtain the power control $PQ_{ref} = PQ_{feed}$ through the direct control of the current $i_{dq\ ref} = i_{dq\ feed}$.

Finally, considering the general model, Equation (6), the command variables are obtained from the dq current control, Equation (7).

$$\begin{aligned} L \frac{di_d}{dt} &= \omega_0 Li_q - Ri_d + V_{td} - V_{sd} \\ L \frac{di_q}{dt} &= -\omega_0 Li_d - Ri_q + V_{tq} - V_{sq} \end{aligned} \quad (6)$$

$$\begin{aligned} V_{td} &= u_d - \omega_0 Li_q + V_{sd} \\ V_{tq} &= u_q + \omega_0 Li_d + V_{sq} \end{aligned} \quad (7)$$

Simple and robust PI current regulators can be used to track references since the dq-axis signals in steady-state are constants (Equation (8)). The result is the controlled model given by Equations (9) and (10), as shown in Figure 4.

$$\begin{aligned} u_d &= \left(k_p + \frac{k_i}{s}\right)(i_{dref} - i_{dfeed}) \\ u_q &= \left(k_p + \frac{k_i}{s}\right)(i_{qref} - i_{qfeed}) \end{aligned} \tag{8}$$

$$\begin{cases} V_{td} = \left(k_p + \frac{k_i}{s}\right)(i_{dref} - i_{dfeed}) - \omega_0 Li_q + V_{sd} \\ V_{tq} = \left(k_p + \frac{k_i}{s}\right)(i_{qref} - i_{qfeed}) + \omega_0 Li_d + V_{sq} \end{cases} \tag{9}$$

$$\begin{cases} L \frac{di_d}{dt} + Ri_d - \omega Li_q = \left(k_p + \frac{k_i}{s}\right) \times (i_d^* - i_d) - \omega Li_q \\ L \frac{di_q}{dt} + Ri_q + \omega Li_d = \left(k_p + \frac{k_i}{s}\right) \times (i_q^* - i_q) + \omega Li_d \end{cases} \tag{10}$$

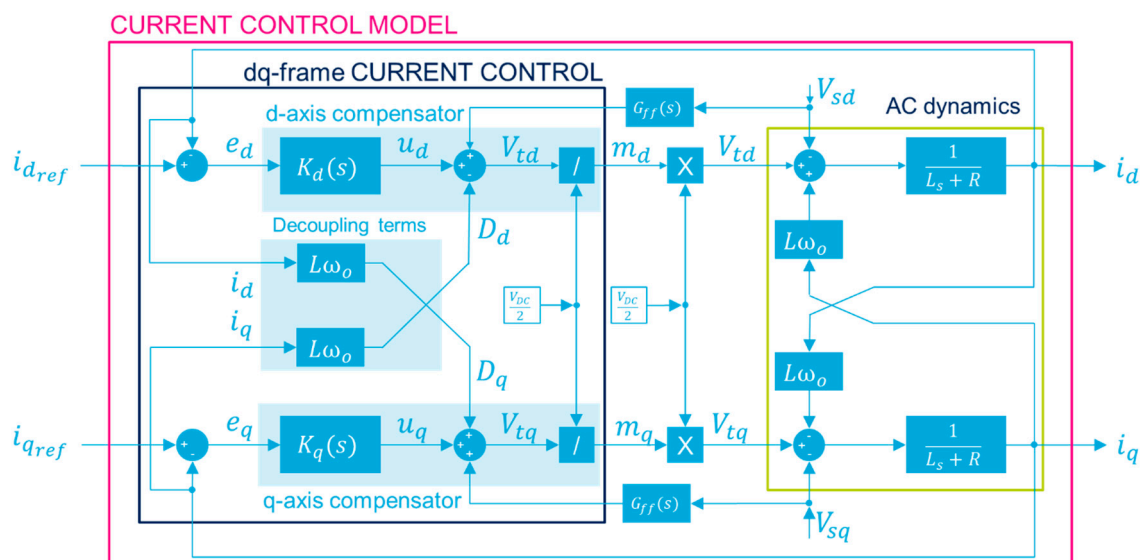


Figure 4. Current control diagram. i_{dqref} current references, e_{dq} current errors, v_{dq} compensator terms, D_{dq} decoupling terms, V_{tdq} control voltages, m_{dq} modulation index.

2.2. Dual Active Bridge

The DAB is the DC/DC isolated bidirectional converter of the BBC (Figure 5). The DAB topology was chosen because of its high efficiency in a wide operating range [27]. It features a symmetrical structure, characterized by two full bridges connected via a high-frequency transformer which also provides galvanic isolation [28]. In Figure 6, a simplified equivalent circuit of the DAB converter is shown. The model of the transformer consists of two elements: the leakage inductor and an ideal transformer that models the voltage ratio. In Figure 7, a simplified circuit where the transformer has been represented on the secondary side to obtain a simple equivalent circuit is shown. The operating states of the converter switches are described in Equation (11).

$$\begin{aligned}
 v_{DAB1}(t) &= \begin{cases} +V_1 & I & T_5, T_8 \text{ on \& } T_6, T_7 \text{ off} \\ 0 & II & T_5, T_7 \text{ on \& } T_6, T_8 \text{ off} \\ -V_1 & IV & T_6, T_7 \text{ on \& } T_5, T_8 \text{ off} \end{cases} \\
 v_{DAB2}(t) &= \begin{cases} +V_2 & I & T_9, T_{12} \text{ on \& } T_{10}, T_{11} \text{ off} \\ 0 & II & T_9, T_{11} \text{ on \& } T_{10}, T_{12} \text{ off} \\ -V_2 & IV & T_{10}, T_{11} \text{ on \& } T_9, T_{12} \text{ off} \end{cases}
 \end{aligned} \tag{11}$$

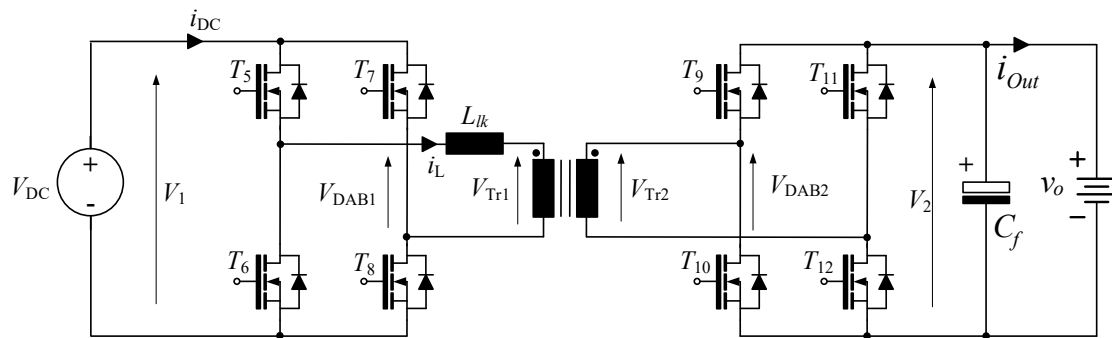


Figure 5. DC/DC stage Dual Active Bridge.

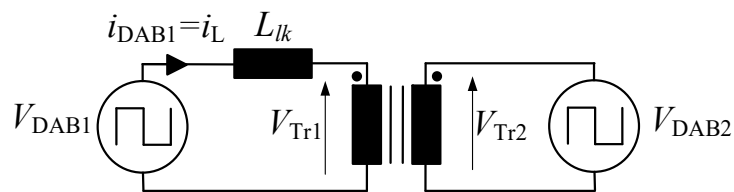


Figure 6. DAB equivalent circuit W/ transformer.

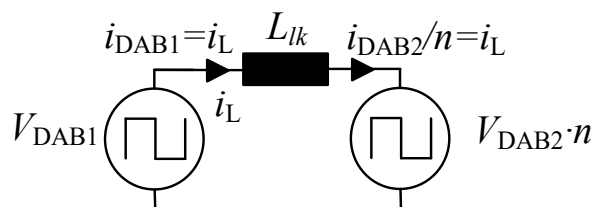


Figure 7. DAB equivalent circuit W/O transformer.

The H-Bridge on the left produces a square-wave voltage with a 50% of duty cycle on the primary side of the transformer. The right-side H-Bridge performs the AC to DC conversion and implements the current control loop used to shape the current charging profile of the battery. The leakage inductance, L_{lk} , plays a key role in the performance of the power conversion. Among the various modulation strategies suggested in the literature, single phase-shift modulation was used to control the power exchange between the BBC and the main grid.

The phase-shift (ϕ) is positive when the power flows from the grid to the battery and negative when it flows in the opposite direction. The relation between the phase-shift and the delivered power is given by Equation (12):

$$P = P_{DAB1} = P_{DAB2} = \frac{nV_1V_2\phi(\pi - |\phi|)}{2\pi^2f_sL_{lk}}, \quad -\pi < \phi < \pi \tag{12}$$

where $-180^\circ < \phi < 180^\circ$, V_1 and V_2 are the input and output voltages of the DAB (Figure 8); n is the transformer turn ratio; f_s is the switching frequency and L_{lk} is the leakage inductance when considering a lossless DAB model.

$P > 0$ denotes a power transfer from DAB1 to DAB2 and $P < 0$ denotes a power transfer from DAB2 to DAB1. The power transfer as a function of the phase-shift is depicted in Figure 8. The related absolute presents two maxima at two different phase-shift angles. The maximum power occurs for $\partial P/\partial \phi = 0$ is:

$$P|P_{max}| = \frac{n V_1 V_2}{8 f_s L_{lk}}, \phi = \pm \frac{\pi}{2} \quad (13)$$

Hence, for a specific active power P , the phase-shift ϕ that must be imposed between the input-output voltages is:

$$\phi = \frac{\pi}{2} \left[1 - \sqrt{1 - \frac{8 f_s L |P|}{n V_1 V_2}} \right] \text{sgn}(P) \quad (14)$$

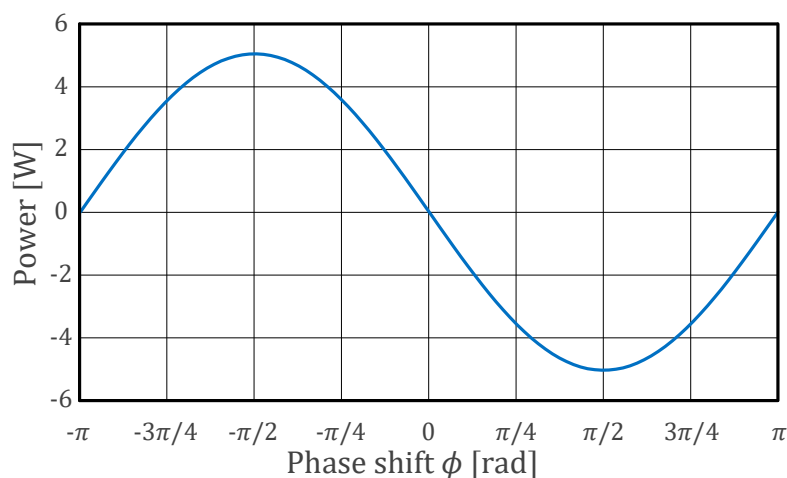


Figure 8. Power transfer vs. Phase-shift.

2.3. High-Frequency Transformer

The high-frequency transformer is responsible for the power transfer and permits to obtain the galvanic isolation [29]. Different core geometries and materials are widespread and the selection of the most appropriate solution mainly depends on the specific application. It is well known that the use of high switching frequency reduces the core size for a given power, while using suitable ferrite materials effectively eliminates eddy currents losses.

The design method is based on the “core geometry method” [30,31].

2.4. Matlab—Simulink Implementation

The model of the BBC and the model of its control were implemented in Matlab-Simulink to simulate the BBC behavior and to evaluate its performance considering different working conditions. The converter model included parasitic elements that affect each power conversion stage. The MOSFETs parameters were considered, as well as the dead-time set in the driving circuit. The closed-loop control block diagram for the AC/DC PFC converter is shown in Figure 9.

Using the Park’s transformation, the regulation was implemented using the i_d and i_q current components to control, respectively, the active and reactive power. This control structure makes it possible to regulate both the DC voltage value and the PF. During G2V mode, the AFE with the PF correction works as an AC to DC converter, and charges the battery while maintaining constant the DC voltage and unitary the PF.

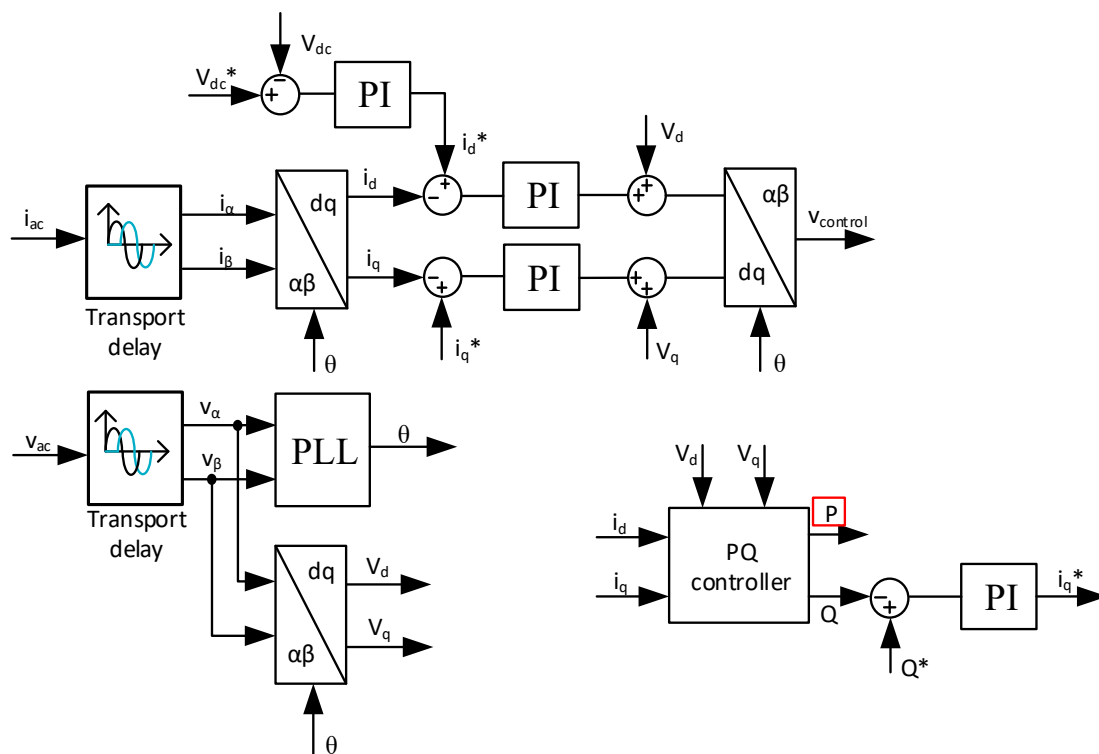


Figure 9. AFE PFC closed-loop control block diagram.

In V2G mode, the battery is discharged and the bridge acts in inverter mode (DC/AC). The control strategy consists of maintaining constant the voltage value on the bus-dc and managing the PF to compensate the amount of reactive power required by the grid. The control loop block diagram for the DAB is shown in Figure 10.

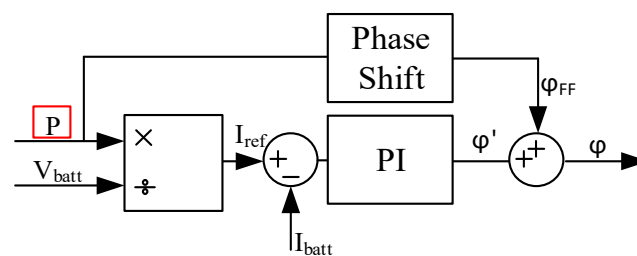


Figure 10. Phase-shift control loop block diagram.

3. Simulation and Validation of the Model of Bidirectional SiC-Based Battery Chargers

A bipolar PWM was implemented with a switching frequency $f_s = 100$ kHz. The switching frequency was selected as the best compromise between efficiency and high power density due to the reduction of the passives composing the AC grid filter and the DC bus link. The modulating signal was evaluated by the voltage grid angle implementing a grid synchronization algorithm setting a unity Power Factor (PF) in G2V or a stable grid synchronization in V2G. The gate signals used to control the SiC MOSFETs were set by the current control loop.

The technical specification of the filter parameters, DC bus link and grid operating conditions considered in the following analysis are listed in Table 1. The design specifications of the DAB of the proposed BBC are listed in Table 2.

Table 1. Technical specification of the AFE parameters.

Parameter	Value
RMS voltage grid	230 V
Grid frequency f_e	50 Hz
L_s	1.5 μ H
Filter parameter C_{ac}	10 μ F
Filter parameter L_c	325 μ H
C_{dc}	400 μ F
Switching frequency f_s	100 kHz

Table 2. DAB design specifications.

Parameter	Value
Nominal input Voltage V_{dc}	400 V
Nominal output voltage V_o	400 V
Minimal output voltage $V_{o,min}$	150 V
Output Power	5 kW
Duty Cycle	0.5
Switching frequency	100 kHz

For this bidirectional converter, the EE core geometry was chosen with N87 material grade. This choice was related to the high switching frequency ($f_s = 100$ kHz) and high-power density of the transformer, whose characteristics are listed in Table 3. An increment in the switching frequency enabled a reduction of passive component size and weight but at the cost of greater switching power losses that, in turn, involve reduced efficiency. Therefore, the adopted frequency was the best compromise for such an application.

Table 3. Technical specification of the transformer parameters.

Parameter	Value
Nominal Input Voltage	400 V
Maximum Input Voltage	480 V
Minimum Input Voltage	360 V
Input current	22 A
Nominal output voltage	400 V
Output Current	17.5 A
Regulation α	0.15%
Max operating flux density B_m	0.16 T
Maximum temperature rise T_r	70 °C

A prototype of the converter was designed and realized using components made by STMicroelectronics to validate the proposed tool by testing the performance and efficiency of the BBC designed using the proposed modelling approach. The power devices are SiC MOSFETs SCT50N120 (Table 4).

Table 4. Power device description: SiC MOSFET SCT50N120.

Symbol	Parameter	Value
V_{DS}	Maximum drain-source voltage	1200 V
I_d	Drain current (continuous) at TC = 25 °C	65 A
$R_{DS(on)}$	Static drain-source on-resistance at 150 °C	59 m Ω
T_j	Max Operating junction temperature in HiP247™	200 °C

A mixed-signal MCUs STM32G474 was used to generate the phase-shift control signal and to manage the dead-time in each power converter leg exploiting the High-Resolution Timer (HRTIM) with

184 ps resolution. The digital control signals were conditioned and applied to the power switches using high-performance gate drivers STGAP2S, a galvanically isolated 4 A single gate drivers. This made it possible to achieve more compact and robust solutions for the entire experimental system.

The modular prototype and the test-bench are shown in Figures 11 and 12.

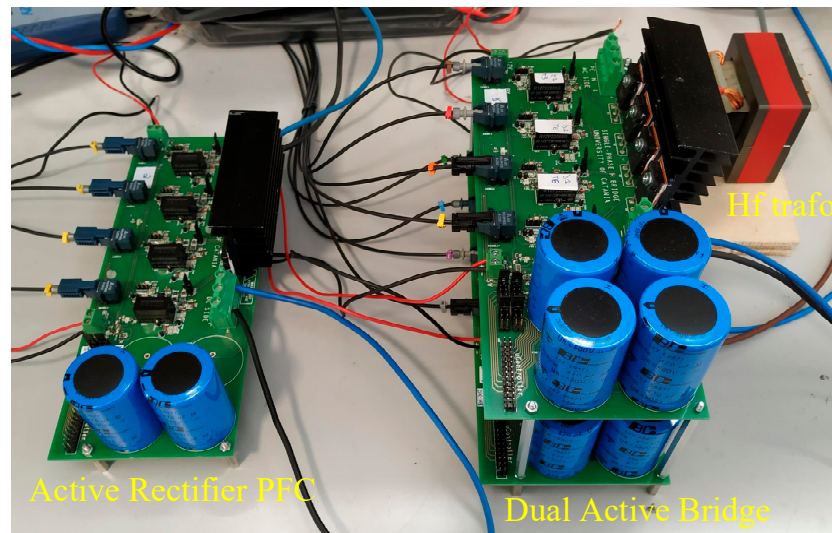


Figure 11. A prototype of the bidirectional battery charger.

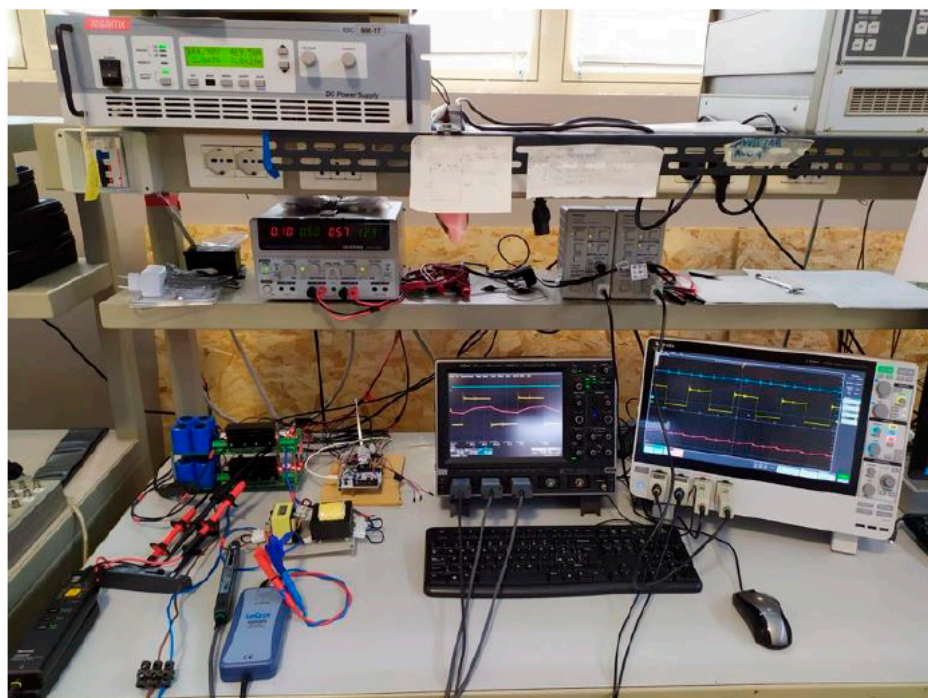


Figure 12. Prototype test-bench.

The power required from the AFE acts on the phase-shift; by varying this reference, it is possible to reverse the power flow. Some simulated and measured waveforms obtained during the G2V mode are shown below. In Figure 13, the simulated first stage waveforms that are the grid voltage v_{ac} and current i_{ac} with unitary PF, and the ripple of the DC voltage are shown. The total harmonic distortion for the AC current was close to 7%, which is in accordance with the value measured (less than 10%) using the prototype.

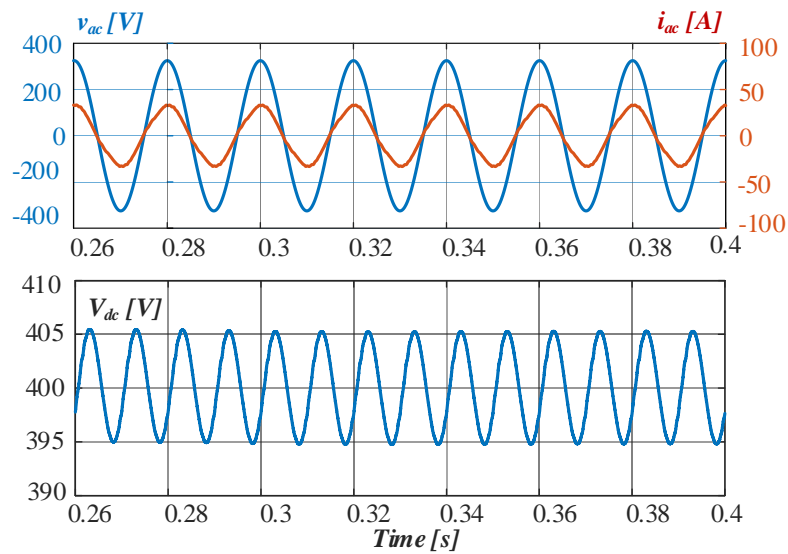
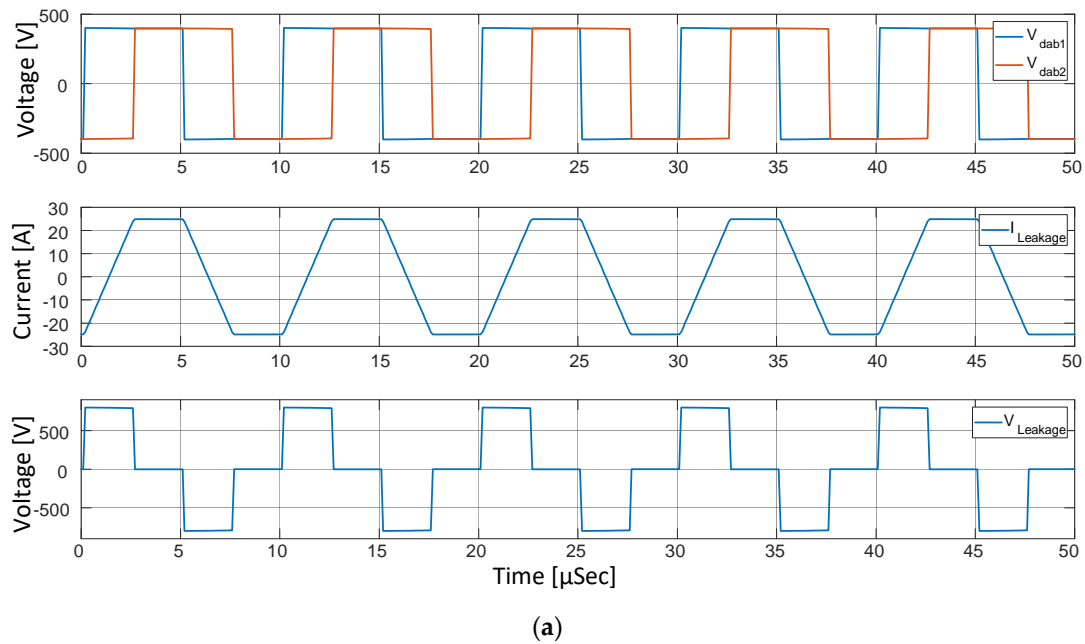


Figure 13. Voltage and current of the AC grid and ripple on the DC side.

The voltage and current on the primary side of the transformer are shown in Figure 14. The simulated waveforms were in good agreement with the measured ones. The main difference was the lack of oscillations in the simulated voltage. These oscillations were due to the coupling between the parasitic capacitance of the devices and the parasitic inductances in the power loop that were neglected in the model. The current waveform depends on the phase-shift between the two transformer-ends voltages. The secondary side quantities were pretty similar, as a turn ratio n equal to one was chosen. The leakage inductance, L_{lk} , affected the power delivered in the DAB converter. Therefore, the voltage v_L waveform was strictly related to the power direction. The DC output waveforms are shown in Figure 15, where the ripple of the voltage V_o and current I_o are highlighted.



(a)

Figure 14. Cont.

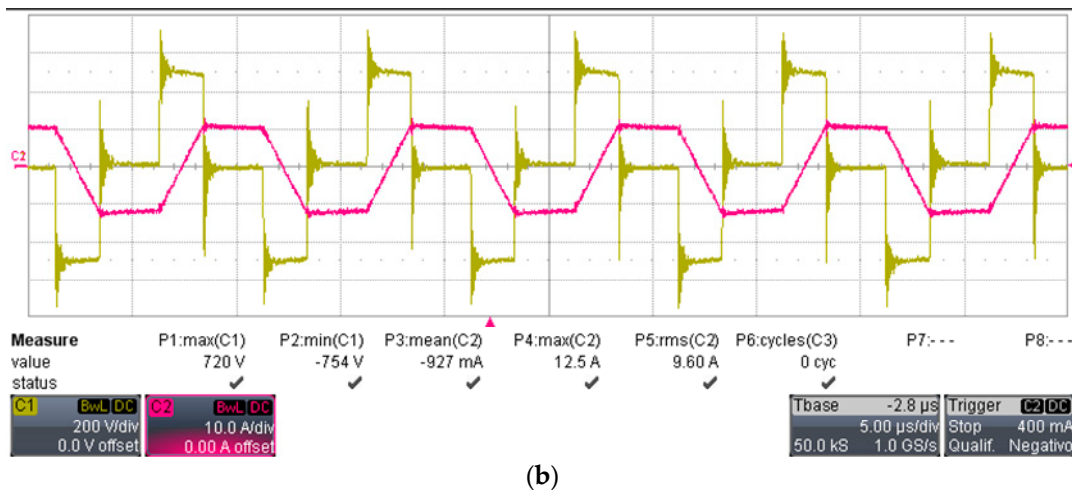


Figure 14. Voltage on both sides of the transformer, voltage and current of the inductance. (a) Simulated waveforms; (b) measured waveforms.

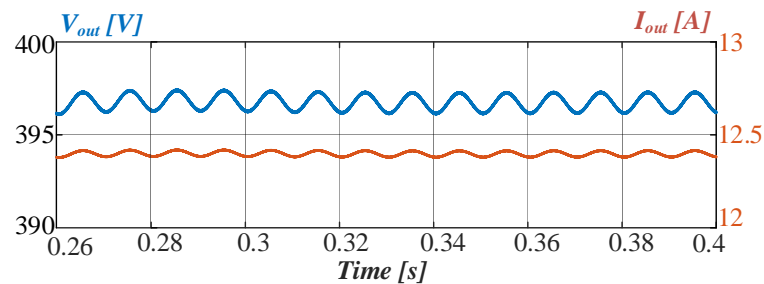


Figure 15. Ripple on the DC output Voltage and Current.

In V2G mode, the power flows from the battery to the grid to satisfy the power demand. In this case, the reference power is modified and acts on the phase-shift value as described above. The transition from G2V to V2G mode at the instant t^* requires current inversion, as illustrated in Figure 16. In this case, the PF has been maintained, meaning that no reactive power was requested by the converter thanks to the proper control. The main simulation results are summarized in Table 5, while in Figure 17, the efficiency of the whole converter is shown.

Table 5. V2G operation—Simulation quantities and results.

Parameter	Value
RMS grid voltage V_s	230 V
RMS grid current I_s	22.6 A
Average Bus DC Voltage V_{dc}	403 V
Average output voltage V_o	397 V
Average output current I_o	12.4 A
Input Apparent Power S	5200 VA
Input Active Power P_{ac}	5200 W
Bus DC Power P_{dc}	5030 W
Output Power P_o	4910 W
Power Factor	0.999
Displacement Power Factor	1
Total Harmonic Distortion	7%
AFE efficiency $\eta = P_{DC}/P_{ac}$	96.7%
DAB efficiency $\eta = P_o/P_{DC}$	97.6%
Power Efficiency $\eta_p = P_o/P_{ac}$	94.42%
Conversion Factor $\eta_c = P_o/S$	94.26%

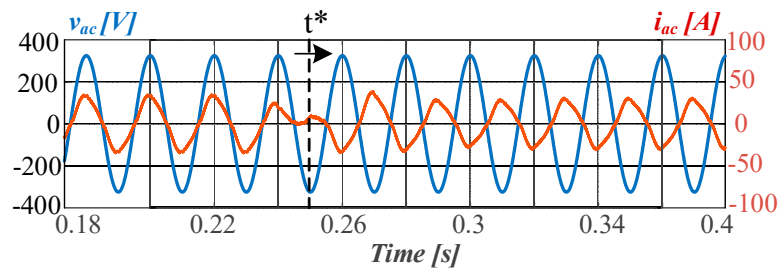
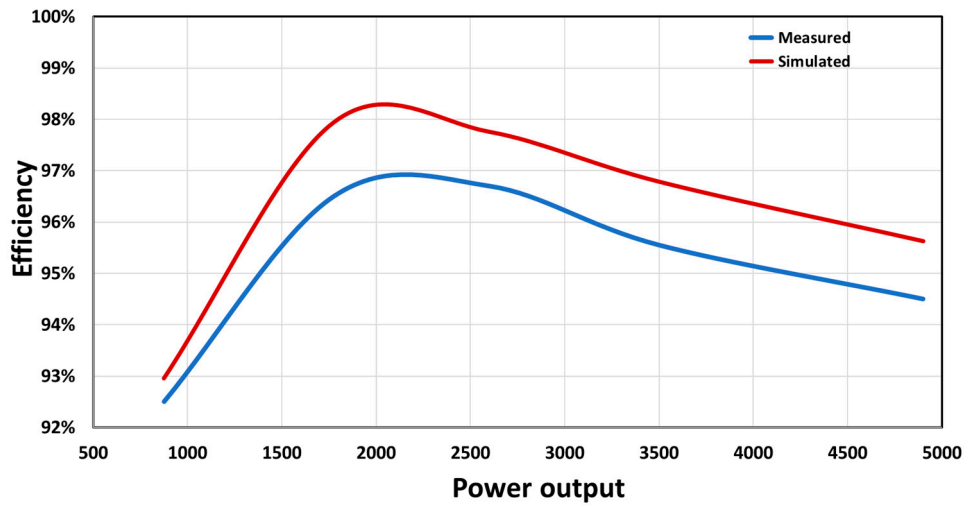
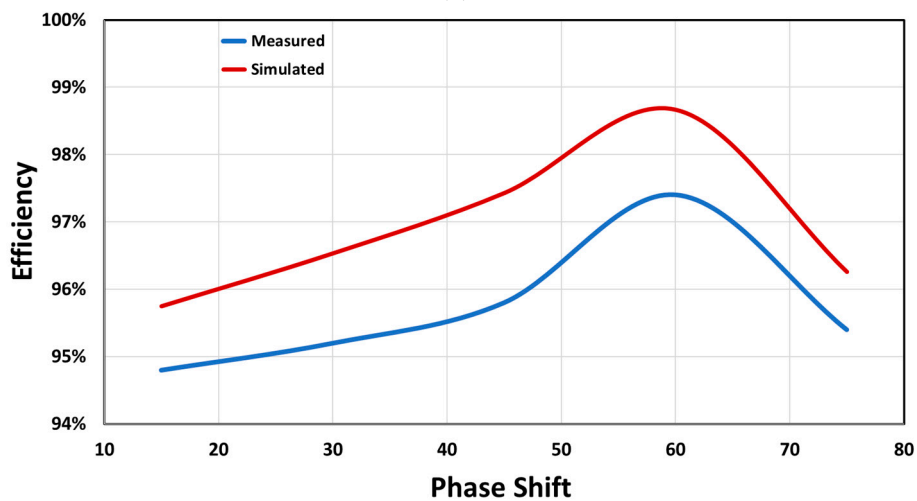


Figure 16. AC voltage and current from G2V to V2G mode.



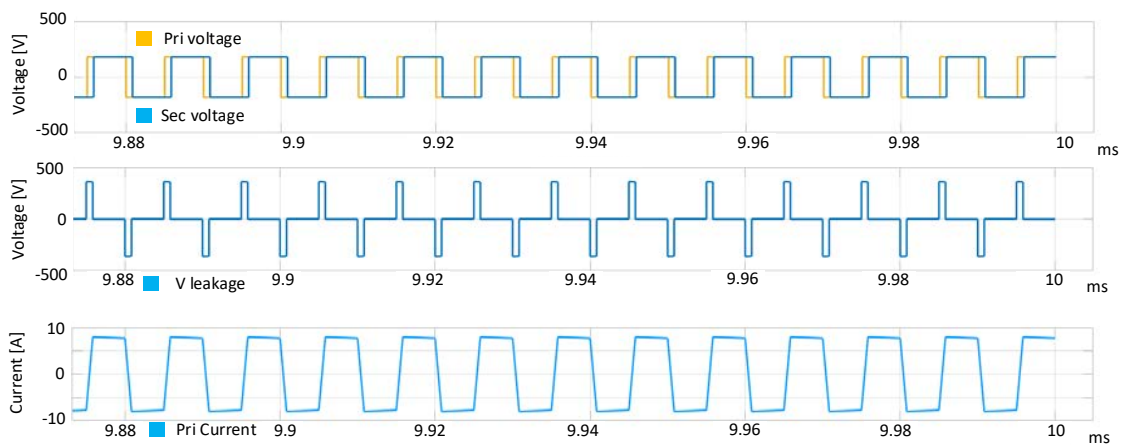
(a)



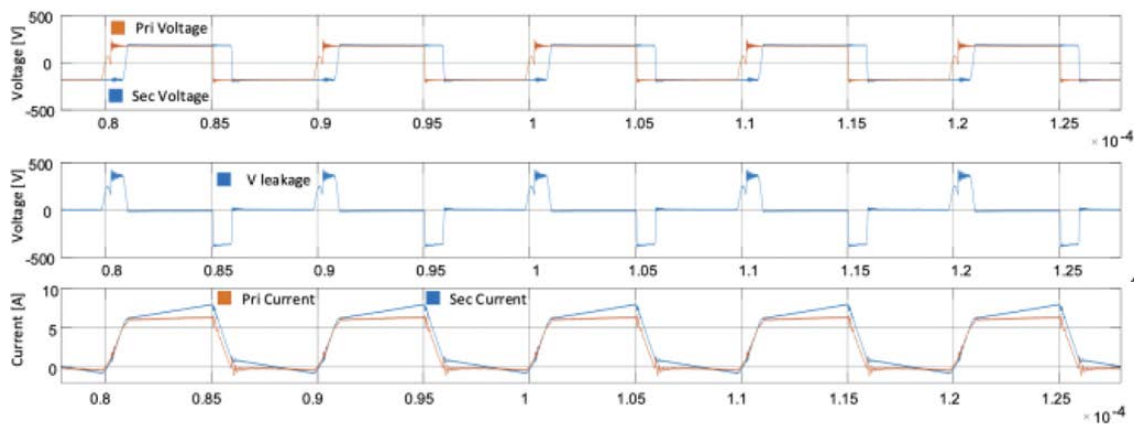
(b)

Figure 17. Efficiency vs. (a) power output and vs. (b) phase shift.

Some other comparisons are reported in Figure 18, confirming the consistency of the proposed modelling approach.



(a)



(b)

Figure 18. DAB: voltage and current waveforms. (a) Simulated (b) Measured.

4. Conclusions

This paper dealt with SiC MOSFET-based BBC with galvanic isolation. A promising topology was studied as the best choice in terms of efficiency, bidirectional power flow management and complexity. The development of an accurate tool accounting for the model of the converter in computer simulator and which was able to exploit FPGA was proposed. It has been shown that this is a suitable approach to design and test the performance of the complex control algorithm, both in G2V with PFC capability and V2G operation modes. The control strategy of the AC/DC converter is composed of a cascade control. One is able to regulate the power flow with the grid, while control of the DC/DC stage consists of the management of the battery charge/discharge. The design and the proposed approach were validated by comparing the simulation results with some experimental tests, confirming the consistency of the proposed method.

Author Contributions: Writing-Review & Editing: G.A., M.C., F.G., S.A.R., G.S. (Giuseppe Scarcella), G.S. (Giacomo Scelba). All authors have read and agreed to the published version of the manuscript.

Funding: This research received no external funding.

Conflicts of Interest: The authors declare no conflict of interest.

Nomenclature

AFE	Active Front End
BBC	Bidirectional Battery Charger
CCM	Continuous Conduction Mode

DAB	Dual Active Bridge
EV	Electric Vehicle
FPGA	Field Programmable Gate Array
GUI	Graphical user interface
HRTIM	High-Resolution Timer
PF	Power Factor
PFC	Power Factor Correction
PHV	Plug-in Hybrid Vehicle
PLL	Phase Locked Loop
SiC	Silicon Carbide
V2G	Vehicle to Grid
ZVS	Zero Voltage Switching
C_{ac}	LCL filter capacitor
C_{dc}	capacitor between the AFE and the DAB
C_f	output capacitor
L_C, L_S	LCL filter inductors
L_{lk}	transformer leakage inductor
i_{α}, i_{β}	two-phase stationary currents
i_d, i_q	two-phase rotating currents
i_{AC}	line current drawn by the converter
i_{Llk}	current flowing through the transformer leakage inductor
i_{out}	output current
v_{out}	output voltage
v_1	DC/DC input voltage
v_2	DC/DC output voltage
$v_{t\alpha}, v_{t\beta}$	two-phase stationary converter voltages
v_{td}, v_{tq}	two-phase rotating converter voltages
$v_{s\alpha}, v_{s\beta}$	two-phase stationary AC main voltages
v_{sd}, v_{sq}	two-phase rotating AC main voltages

References

- Shi, J.; Gao, Y.; Wang, W.; Yu, N.; Ioannou, P.A. Operating Electric Vehicle Fleet for Ride-Hailing Services with Reinforcement Learning. *IEEE Trans. Intell. Transp. Syst.* **2020**, *21*, 4822–4834. [[CrossRef](#)]
- Neffati, A.; Marzouki, A. Local energy management in hybrid electrical vehicle via Fuzzy rules system. *AIMS Energy* **2020**, *8*, 421–437. [[CrossRef](#)]
- Dominkovic, D.F.; Bačeković, I.; Pedersen, A.S.; Krajačić, G. The future of transportation in sustainable energy systems: Opportunities and barriers in a clean energy transition. *Renew. Sustain. Energy Rev.* **2018**, *82*, 1823–1838. [[CrossRef](#)]
- Franco, F.L.; Ricco, M.; Mandrioli, R.; Grandi, G. Electric Vehicle Aggregate Power Flow Prediction and Smart Charging System for Distributed Renewable Energy Self-Consumption Optimization. *Energies* **2020**, *13*, 5003. [[CrossRef](#)]
- Vadi, S.; Bayindir, R.; Colak, A.M.; Hossain, E. Vadi A Review on Communication Standards and Charging Topologies of V2G and V2H Operation Strategies. *Energies* **2019**, *12*, 3748. [[CrossRef](#)]
- Salvatti, G.A.; Carati, E.G.; Cardoso, R.; Da Costa, J.P.; Stein, C.M.D.O. Electric Vehicles Energy Management with V2G/G2V Multifactor Optimization of Smart Grids. *Energies* **2020**, *13*, 1191. [[CrossRef](#)]
- Juul, F.; Negrete-Pincetic, M.; Macdonald, J.; Callaway, D. Real-time scheduling of electric vehicles for ancillary services. In Proceedings of the 2015 IEEE Power & Energy Society General Meeting, Denver, CO, USA, 26–30 July 2015; pp. 1–5.
- Liu, C.; Chau, K.T.; Wu, D.; Gao, S. Opportunities and Challenges of Vehicle-to-Home, Vehicle-to-Vehicle, and Vehicle-to-Grid Technologies. *Proc. IEEE* **2013**, *101*, 2409–2427. [[CrossRef](#)]
- Kisacikoglu, M.C.; Ozpineci, B.; Tolbert, L.M. EV/PHEV Bidirectional Charger Assessment for V2G Reactive Power Operation. *IEEE Trans. Power Electron.* **2013**, *28*, 5717–5727. [[CrossRef](#)]

10. Kisacikoglu, M.C.; Kesler, M.; Tolbert, L.M. Single-Phase On-Board Bidirectional PEV Charger for V2G Reactive Power Operation. *IEEE Trans. Smart Grid* **2015**, *6*, 767–775. [[CrossRef](#)]
11. Xue, L.; Shen, Z.; Boroyevich, D.; Mattavelli, P.; Diaz, D. Dual Active Bridge-Based Battery Charger for Plug-in Hybrid Electric Vehicle with Charging Current Containing Low Frequency Ripple. *IEEE Trans. Power Electron.* **2015**, *30*, 7299–7307. [[CrossRef](#)]
12. De Caro, S.; Testa, A.; Triolo, D.; Cacciato, M.; Consoli, A. Low input current ripple converters for fuel cell power units. In Proceedings of the 2005 European Conference on Power Electronics and Applications, Dresden, Germany, 11–14 September 2005.
13. De Melo, H.N.; Trovao, J.P.F.; Pereirinha, P.G.; Jorge, H.M.; Antunes, C.H. A Controllable Bidirectional Battery Charger for Electric Vehicles with Vehicle-to-Grid Capability. *IEEE Trans. Veh. Technol.* **2017**, *67*, 114–123. [[CrossRef](#)]
14. Restrepo, M.; Morris, J.; Kazerani, M.; Canizares, C. Modeling and Testing of a Bidirectional Smart Charger for Distribution System EV Integration. *IEEE Trans. Smart Grid* **2016**, *9*, 152–162. [[CrossRef](#)]
15. Raciti, A.; Musumeci, S.; Chimento, F.; Privitera, G. A new thermal model for power MOSFET devices accounting for the behavior in unclamped inductive switching. *Microelectron. Reliab.* **2016**, *58*, 3–11. [[CrossRef](#)]
16. Mohammed, S.S.; Devaraj, D. Simulation and analysis of stand-alone photovoltaic system with boost converter using MATLAB/Simulink. In Proceedings of the 2014 International Conference on Circuits, Power and Computing Technologies [ICCPCT-2014], Nagercoil, India, 20–21 March 2014; pp. 814–821.
17. Doola, S.; Bhat, S.S.; Bhatti, T.; Veerachary, M. A GUI based simulation of power electronic converters and reactive power compensators using MATLAB/SIMULINK. In Proceedings of the 2004 International Conference on Power System Technology, The Pan Pacific, Singapore, 21–24 November 2004.
18. Aiello, G.; Cacciato, M.; Scarcella, G.; Scelba, G.; Gennaro, F.; Aiello, N. RealTime emulation of a three-phase vienna rectifier with unity power factor operations. In Proceedings of the 2018 ELEKTRO, Mikulov, Czech Republic, 21–23 May 2018.
19. Aiello, G.; Scelba, G.; Scarcella, G.; Cacciato, M.; Tornello, L.; Palmieri, A.; Vanelli, E.; Pernaci, C.; Di Dio, R. Real-Time Emulation of Induction Machines for Hardware in the Loop Applications. In Proceedings of the 2018 International Symposium on Power Electronics, Electrical Drives, Automation and Motion (SPEEDAM), Amalfi, Italy, 20–22 June 2018.
20. Aiello, G.; Tornello, L.D.; Scelba, G.; Scarcella, G.; Cacciato, M.; Palmieri, A.; Vanelli, E.; Pernaci, C.; Di Dio, R. FPGA-Based Design and Implementation of a Real Time Simulator of Switched Reluctance Motor Drives. In Proceedings of the 2019 21st European Conference on Power Electronics and Applications (EPE '19 ECCE Europe), Genova, Italy, 2–5 September 2019.
21. Scelba, G.; Scarcella, G.; Cacciato, M.; Aiello, G. Hardware in the loop for failure analysis in AC motor drives. In Proceedings of the 2016 ELEKTRO, Strbske Pleso, Slovakia, 16–18 May 2016.
22. Acquaviva, A.; Thiringer, T. Energy efficiency of a SiC MOSFET propulsion inverter accounting for the MOSFET's reverse conduction and the blanking time. In Proceedings of the 2017 19th European Conference on Power Electronics and Applications (EPE'17 ECCE Europe), Warsaw, Poland, 11–14 September 2017.
23. Gritti, G.; Adragna, C.; Industrial & Power Conversion Division Application Laboratory—STMicroelectronics s.r.l.—via C. Olivetti 2—20864 Agrate Brianza (MB)—Italy. Analysis, design and performance evaluation of an LED driver with unity power factor and constant-current primary sensing regulation. *AIMS Energy* **2019**, *7*, 579–599. [[CrossRef](#)]
24. Chimento, F.; Raciti, A.; Cannone, A.; Musumeci, S.; Gaito, A. Parallel connection of super-junction MOSFETs in a PFC application. In Proceedings of the 2009 IEEE Energy Conversion Congress and Exposition, San Jose, CA, USA, 20–24 September 2009; pp. 3776–3783.
25. Yazdani, A.; Iravani, R. *Voltage-Sourced Converters in Power Systems: Modeling, Control, and Applications*; John Wiley & Sons: Hoboken, NJ, USA, 2010.
26. Cacciato, M.; Scarcella, G.; Scelba, G.; Finocchiaro, L. Multi-reference frame based PLL for single phase systems in voltage distorted grids. In Proceedings of the 2014 16th European Conference on Power Electronics and Applications, EPE-ECCE Europe 2014, Lappeenranta, Finland, 26–28 August 2014.
27. Jafari, M.; Malekjamshidi, Z.; Zhu, J.G. Analysis of operation modes and limitations of dual active bridge phase shift converter. In Proceedings of the 2015 IEEE 11th International Conference on Power Electronics and Drive Systems, Sydney, Australia, 9–12 June 2015.

28. Cacciato, M.; Consoli, A. New regenerative active snubber circuit for ZVS phase shift Full Bridge converter. In Proceedings of the 2011 Twenty-Sixth Annual IEEE Applied Power Electronics Conference and Exposition (APEC), Fort Worth, TX, USA, 6–11 March 2011.
29. Alves Ferreira Júnior, A.; Justino-Ribeiro, J.; Ney do Amaral Pereira, W. Evaluating Impedance Transformers with a VNA. *Microwaves Rf* **2009**, *48*, 64–71. Available online: https://www.researchgate.net/publication/243055235_Evaluating_Impedance_Transformers_With_a_VNA/references (accessed on 10 October 2020).
30. Barrios, E.L.; Ursua, A.; Marroyo, L.; Sanchis, P. Analytical Design Methodology for Litz-Wired High-Frequency Power Transformers. *IEEE Trans. Ind. Electron.* **2015**, *62*, 2103–2113. [[CrossRef](#)]
31. Hoang, K.D.; Wang, J. Design optimization of high frequency transformer for dual active bridge DC-DC converter. In Proceedings of the 2012 XXth International Conference on Electrical Machines, Marseille, France, 2–5 September 2012.

Publisher’s Note: MDPI stays neutral with regard to jurisdictional claims in published maps and institutional affiliations.



© 2020 by the authors. Licensee MDPI, Basel, Switzerland. This article is an open access article distributed under the terms and conditions of the Creative Commons Attribution (CC BY) license (<http://creativecommons.org/licenses/by/4.0/>).